Flow Reduction due to Degassing and Redissolution Phenomena

Christine Doughty
Earth Sciences Division
Lawrence Berkeley Laboratory

Introduction

At the Stripa mine in Sweden, flow and transport experiments in a water-saturated fractured granite were conducted to investigate techniques for site characterization for a geologic nuclear waste repository. In the Simulated Drift Experiment, measured water inflow to an excavated drift with pressure held at 1 bar was only 1/9th the value expected based on inflow to boreholes with pressure held at 2.7 bars [*Olsson*, 1992]. Several physical and chemical mechanisms were hypothesized to be responsible for this reduction in flow [*Long et al.*, 1992]. One possibility is that significant degassing of dissolved nitrogen takes place between 2.7 and 1 bars, creating a two-phase regime with an accompanying decrease in fluid mobility, resulting in a decrease in flow to the drift. To investigate this process, theoretical studies on degassing and redissolution phenomena have been carried out, beginning with an idealized model which yields a simple analytical solution, then relaxing some of the simplifying assumptions and using TOUGH2 to study the phenomena numerically. In conjunction with these theoretical studies, laboratory experiments on flow and degassing in transparent fracture replicas are being carried out [*Geller et al.*, 1995], and are being used to check the modeling approach. We need to develop a fundamental understanding of degassing and redissolution in particular and two-phase flow phenomena in general for flow in fractures and fracture networks, in order to successfully model conditions around a nuclear waste repository, where long time and large space scales may preclude conclusive field experiments.

Analytical Solution

For one-dimensional steady-state flow through a homogeneous medium, there is a simple analytical expression that gives an upper bound to the flow reduction that can be caused by degassing. Here one-dimensional means that there is only one spatial dimension in the problem, but the flow geometry can be linear ($n = 1$), radial ($n = 2$), spherical ($n = 3$), or the non-integral geometries characteristic of some fracture networks. The effect of gravity is neglected. Darcy's law governs fluid flow, and while the exact form of the characteristic curves need not be specified, there must be strong interference between phases. In general, strong interference is expected for flow through low-dimensional flow regimes (e.g., flow through highly channelized fractures would exhibit more interference than flow through an isotropic porous medium). Thermodynamic equilibrium between gas dissolved in the liquid phase and gas existing as a separate gas phase is assumed, and is governed by Henry's law. When pressure falls below the bubble pressure P_b, dissolved gas comes out of solution and forms a separate gas phase, whereas above P_b, gas remains in solution and single-phase liquid conditions prevail. According to Henry's law, P_b is directly proportional to gas content, defined as the mole fraction of gas dissolved in the liquid phase. Gas content can also be expressed as a mass fraction or as a volume percent at STP.

The pressure is assumed to be held fixed at both ends of a medium of length L, at one end below the bubble pressure (P_0), and at the other end above it (P_1). The upper frame of Figure 1 shows the pressure variation under degassing conditions schematically. For strongly interfering relative permeability curves, a steep pressure gradient is required to drive flow through the two-phase region, whose width l is rather small. The flow reduction due to degassing can be quantified by a normalized flow $\tilde{q}$, defined as the flow through the medium with gas present (q), divided by the flow through the medium under the same boundary conditions if no gas were present (q_0). According to Darcy's law, the normalized flow is simply the ratio of the slopes of the liquid-phase portion of the pressure curves:

$$\tilde{q} = \frac{q}{q_0} = \frac{(P_1 - P_b)/(L - l)}{(P_1 - P_0)/L} . \tag{1}$$

In the limit $l \ll L$ this becomes

$$\tilde{q} \approx \frac{P_1 - P_b}{P_1 - P_0} . \tag{2}$$

Figure 1 and Equation (2) illustrate how the interplay of gas content (as represented by P_b), and boundary conditions (P_1 and P_0) controls the flow reduction. In the context of the Stripa field experiment, P_1 is the far-field pressure, and P_0 is the pressure at the drift. The lower frame of Figure 1 shows the normalized flow as predicted by Equation (1) and the results for the Stripa Simulated Drift Experiment (SDE), and indicates that not nearly enough flow reduction is predicted by the analytical solution ($\tilde{q}_{an} = 0.92$ as opposed to $\tilde{q}_{obs} = 0.11$). The analytical solution was verified against numerical results using the TOUGH2 simulator [*Pruess*, 1987, 1991], and the effect of the choice of characteristic curves was studied numerically. Using relative permeability functions with weaker phase interference produced less flow reduction, as did the addition of capillary pressure. While expected on physical grounds, these findings did not improve the prediction of the Stripa SDE results or subsequent comparisons with laboratory results [*Geller et al.*, 1995], which were consistent with the Stripa SDE results. Therefore, a further examination of the assumptions used for the analytical solution was warranted, which required investigating the degassing and redissolution problem numerically.

Numerical Homogeneous Media Studies

By using TOUGH2 to examine the degassing problem numerically, both transient and steady-state conditions can be studied. In addition, the effect of the far-

field constant pressure boundary condition can be examined, by considering both finite and infinite systems. Under these conditions, the flow geometry has a tremendous effect not only on flow reduction, but on whether a steady-state develops at all. In a fractured rock mass the flow geometry is very complicated, as it depends on both the nature of the flow channels within a single fracture plane, and the connectivity of the network of fracture planes. However, simple models using either linear, cylindrical, or spherical flow geometries provide insight into limiting cases of possible flow geometries in a real rock mass. Figures 2, 3, and 4 show $\tilde{q}$ versus time for linear, radial, and spherical flow geometries, for finite and infinite systems. In all cases, the q_0 value used to normalize q is the steady-state value for a finite system. Time is normalized by t_{diff}, the time required for a pressure pulse to diffuse across the finite medium under liquid-phase conditions.

The $\tilde{q}$ value given by the analytical solution, shown as a symbol at the final time, agrees reasonably well with the numerically calculated values. The difference between finite and infinite systems decreases strikingly as flow dimension increases, because pressure changes become more localized around the borehole. For linear geometry, no steady state develops for an infinite system, whereas for radial geometry a quasi-steady state develops, and for spherical geometry there is no difference between finite and infinite systems. For linear geometry and an infinite medium (Figure 2), flow rates decline monotonically to zero. Because compressibility increases with gas content, the decline occurs at later times for greater gas contents. Thus at any given time, degassing causes a flow increase rather than reduction. For radial geometry (Figure 3) the difference between finite and infinite media is still apparent, but in both cases greater gas content causes greater flow reduction. The time required to reach steady state decreases as flow dimension increases, but increases strongly with gas content.

One of the powerful features of the integral finite difference method for spatial discretization which is employed in TOUGH2 is the ability to create efficient computational meshes for arbitrary flow geometries very easily. A mesh generator has been developed that creates a one-dimensional mesh with arbitrary flow dimension ranging from $n = 1$ (linear) to $n = 3$ (spherical). This mesh was used not only for the calculations illustrated above for $n = 1$, $n = 2$, and $n = 3$, but also to create meshes with non-integral flow dimensions of $n = 1.4$ and $n = 2.4$, which may be used to represent incompletely connected fracture networks. Figure 5 shows $\tilde{q}$ versus time for $n = 1.4$. As expected, the variation in $\tilde{q}$ is intermediate between that for $n = 1$ and $n = 2$, whereas the variation for $n = 2.4$ (not shown) is intermediate between $n = 2$ and $n = 3$.

In conclusion, relaxing the assumptions of the analytical solution did not improve the model's prediction of the Stripa SDE results or those of laboratory experiments. However, the numerical solution verified the essential features of the analytical solution. Firstly, if a steady-state value of $\tilde{q}$ exists (finite media for linear or radial flow geometries, finite or infinite media for spherical flow geometry), it is independent of flow dimension.

Secondly, flow reduction increases as gas content increases. The steady-state flow reduction predicted by the numerical simulations generally agrees with the analytical solution, but as the amount of gas present increases, the analytical solution approximation gets worse.

Numerical Heterogeneous Media Studies

All the numerical simulations described above considered a homogeneous medium characterized by a single value of permeability. However, laboratory experiments being conducted with fracture replicas indicate that heterogeneity within the flow domain has an important effect on the magnitude of flow reduction [*Geller et al.*, 1995]. Therefore, a two-dimensional numerical model of a fracture replica was created in order to examine the effect of a heterogeneous medium on flow reduction. The fracture replica is about 74 mm on a side and the aperture distribution is given as a 369 by 369 array of aperture values, each representing a 0.02 mm by 0.02 mm square. Aperture values range from 0 (an asperity) to 240 microns. Using these values directly would result in a model with over 130,000 elements, which would be impractical for numerical simulation. After some study, it was decided to arithmetically average over 9 by 9 blocks of adjacent aperture values to obtain a 41 by 41 array of aperture values, each representing a 0.18 mm by 0.18 mm square. This results in a model with 1681 elements representing the fracture replica (Figure 6) and an additional 82 elements representing the constant-pressure boundaries. Doing harmonic or geometric averaging rather than arithmetic averaging did not make much difference in the averaged aperture distribution, and using a more finely discretized 123 by 123 array of apertures (averaging over 3 by 3 blocks) did not greatly alter the nature of the heterogeneity. The averaged aperture values were divided into eight ranges, and the element aperture value was assigned as the midpoint of the range minus 25 microns, a somewhat arbitrary value chosen to enhance the effects of asperities.

The cubic law was then used to determine the permeability of the element. Modified van Genuchten characteristic curves which exhibited strong phase interference ($\lambda = 0.4$) were employed, using the same relative permeability functions for each element and a capillary pressure strength inversely proportional to aperture.

A numerical simulation of flow from right to left through the model was done to compare with a laboratory experiment using the same flow geometry. Initial conditions consisted of a single-phase liquid at a uniform pressure of 5 bars, with a dissolved gas mass fraction of 7×10^{-5} (5% gas by volume at STP), which corresponds to a bubble pressure of 3.1 bars. The pressure was held fixed at 5 bars at the right side of the flow domain and 1 bar at the left side; the top and bottom boundaries were closed.

Figure 7 shows the variation of normalized flow $\tilde{q}$ with time for both the model with asperities and an earlier version of the model without asperities and less resolution of small apertures. Both simulations required over 800 time steps to reach steady state. The oscillation in

228

flow rate that is seen before steady-state conditions are reached suggests that there are multiple physical processes occurring on different time scales, which generally makes numerical simulation difficult. In particular, the use of strongly interfering relative permeability curves forces TOUGH2 to take small time steps in order for the Newton-Raphson iterations to converge. This occurs because a small increase in gas saturation due to degassing can cause a large decrease in fluid mobility, which results in a large decrease in flow rate, and hence a significant build-up of pressure up-gradient of the degassing location. When pressure increases above the bubble pressure, gas is redissolved, liquid relative permeability increases, fluid flow rate increases, and pressure decreases, setting the stage for degassing to resume, repeating the cycle. Thus, it is the intrinsic physics of the problem, which involves a subtle balance of forces, that makes the problem difficult to numerically simulate. Only the direct solver MA28, which is generally slower but more robust than the conjugate gradient solvers, could be used to reach steady state. Use of MA28 also limits the resolution of the fracture aperture distribution that may be achieved, as the maximum number of elements and connections is much smaller than for the conjugate gradient methods.

Figure 7 shows that the decrease in apertures which resulted from the addition of asperities decreases flow whether or not gas is present, as expected based on the cubic law. However, the steady-state normalized flow $\tilde{q}$ does not change. The final normalized flow value is slightly larger than the analytical solution, and not nearly as small as laboratory values using this fracture replica, indicating that simply adding heterogeneity to the model is insufficient to produce a significantly greater flow reduction.

The modeled steady-state pressure and gas-saturation distributions are shown in Figure 8. As expected, variations in the aperture distribution are manifested in the pressure distribution, such as the greater variability in aperture in the left half of the model resulting in greater irregularities in the pressure contours. Furthermore, there is a close correspondence between pressure and saturation distributions, with two-phase conditions occurring only below the bubble pressure. The gas saturation distribution shown in Figure 8 compares favorably with the experimental gas distribution, which is shown in Figure 9, indicating that some features of the actual fracture replica are being represented correctly in the numerical model, despite the incorrect prediction of $\tilde{q}$. The earlier version of the model, which did not resolve the small-aperture distribution, did not reproduce the observed saturation distribution nearly as well.

Several other variations on the numerical model of flow through the fracture replica were made, but none predicted a greater flow reduction than given by the analytical solution. These variations included using a different gas content, a uniform aperture distribution, a non-zero irreducible gas saturation, modeling flow in the opposite direction through the fracture replica, and varying the choice of characteristic curves.

Conclusions and Plans for Future Work

Our theoretical study began with a simple analytical solution for the flow reduction due to degassing under steady-state conditions in a finite one-dimensional homogeneous medium. When this solution did not predict laboratory or field conditions adequately, some the assumptions required for the analytical solution were relaxed and the problem was numerically simulated using TOUGH2. In particular, the model was extended from steady-state to transient conditions, finite to infinite media, from linear to radial, spherical, and non-integral flow geometries, and from a homogeneous medium to a heterogeneous medium. None of the extensions to the conceptual model has significantly increased the flow reduction due to degassing from that predicted by the analytical solution. Hence all the modeling studies significantly underpredict the effect of degassing on fluid flow measured in the laboratory and at the Stripa SDE. The next assumption to be investigated is that of equilibrium between degassing and redissolution. Adding non-equilibrium effects to TOUGH2 will be a significant effort, and three possible approaches are being considered. In order of increasing complexity (and rigor) they are: to consider degassing only, with no redissolution possible; to use a hysteretic form of Henry's law which makes degassing occur more readily than dissolution; and to use kinetic rate equations for both degassing and dissolution.

References

Geller, J.T., C. Doughty, R.J. Glass, and J.C.S. Long, Disturbed zone effects: two-phase flow, report to the international program under the cooperative agreement between SKB and U.S. DOE Radioactive Waste Management, *Rep. LBL-36848*, Lawrence Berkeley Laboratory, Berkeley, Calif, 1995.

Long, J.C.S., O. Olsson, S. Martel, J. Black, Effects of excavation on water inflow to a drift, in Proceedings of the U.S. Rock Mechanics Meeting, Lake Tahoe, Calif, 1992.

Olsson, O., ed, Site characterization and validation - final report, Stripa Project Technical Report 92-22, Swedish Nuclear Fuel and Waste Management Co., Stockholm Sweden, 364 pp., 1992.

Pruess, K., TOUGH user's guide, *Rep. LBL-20700*, Lawrence Berkeley Lab., Berkeley, Calif, 1987.

Pruess, K., TOUGH2 - A general-purpose numerical simulator for multiphase fluid and heat flow, *Rep. LBL-29400*, Lawrence Berkeley Lab., Berkeley, Calif, 1991.

Figure 3. Normalized flow $\tilde{q}$ as a function of normalized time for radial flow geometry ($n = 2$), finite and infinite media, and various gas contents.
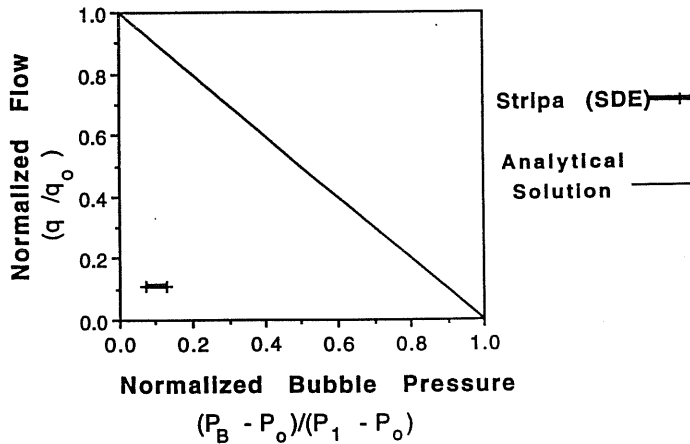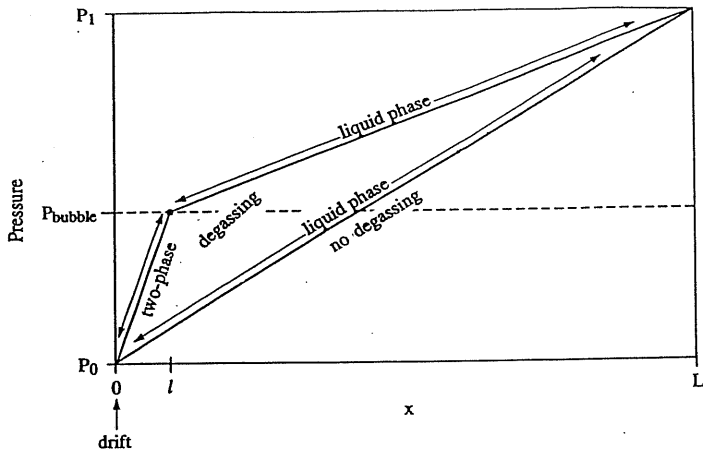

Figure 1. Top frame: conceptual model of flow reduction due to degassing for steady-state flow through a one-dimensional homogeneous medium with pressure held fixed at either end. Bottom frame: normalized flow versus normalized gas content for the analytical solution and the Stripa SDE result.
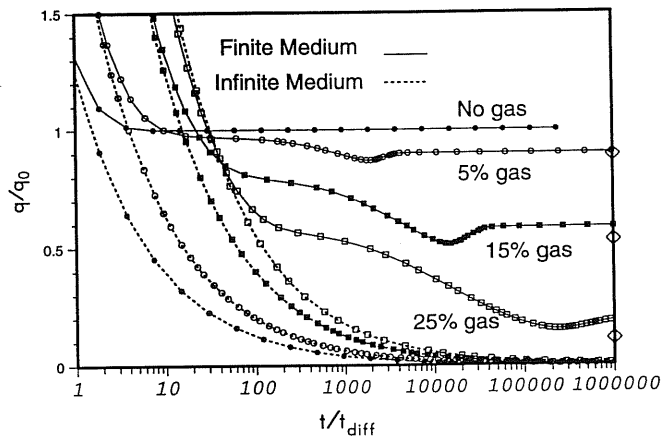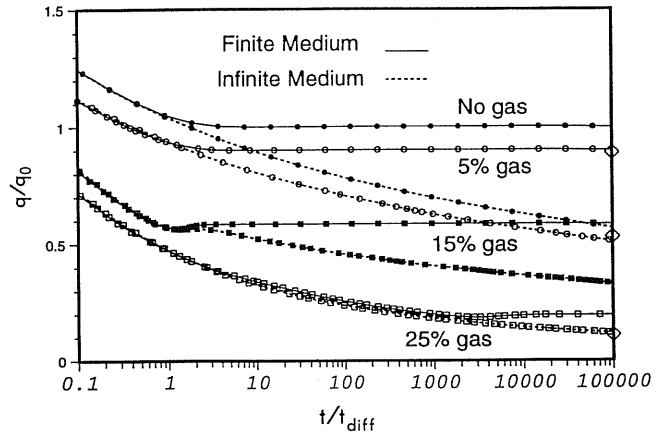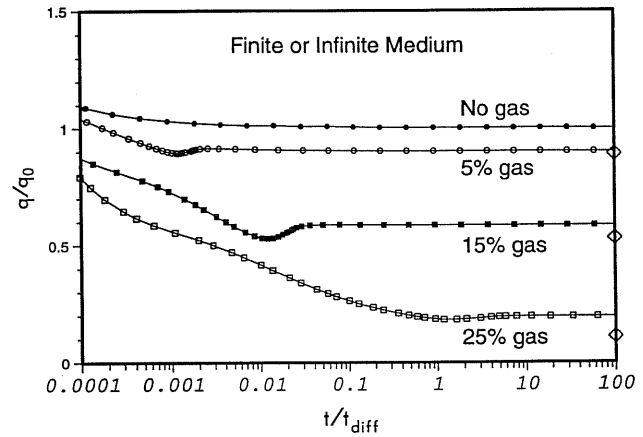
Figure 4. Normalized flow $\tilde{q}$ as a function of normalized time for spherical flow geometry ($n = 3$), finite and infinite media, and various gas contents.

Figure 2. Normalized flow $\tilde{q}$ as a function of normalized time for linear flow geometry ($n = 1$), finite and infinite media, and various gas contents.
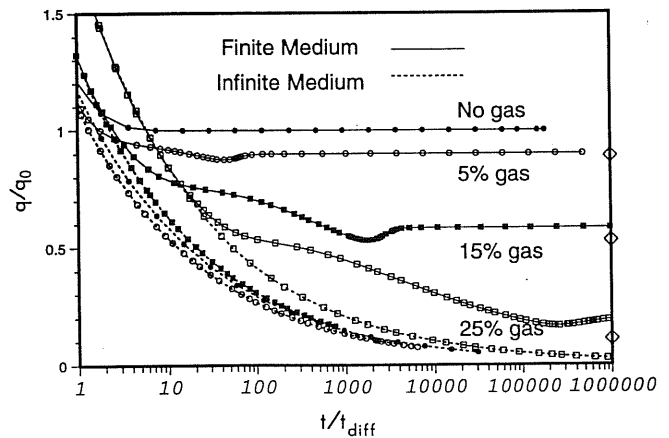
Figure 5. Normalized flow $\tilde{q}$ as a function of normalized time for non-integral flow geometry between linear and radial ($n = 1.4$), finite and infinite media, and various gas contents.
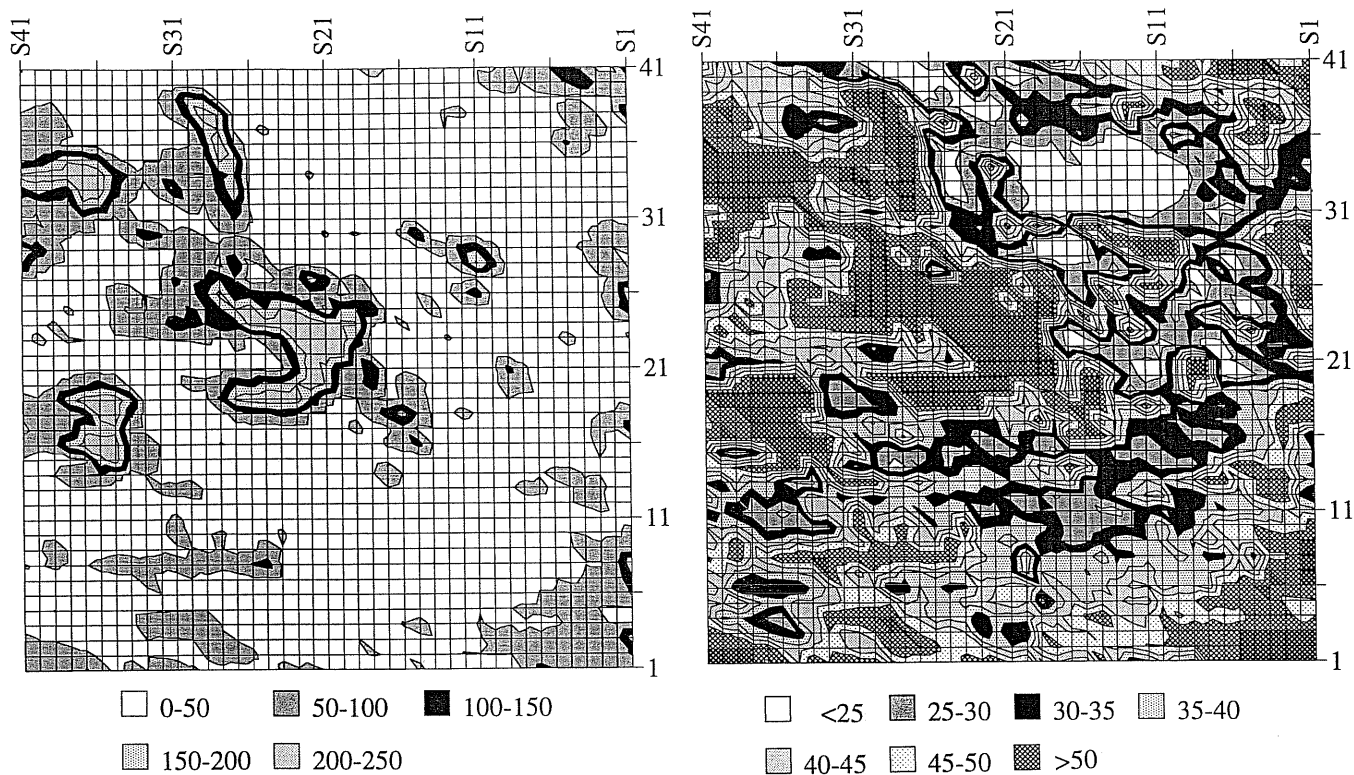
230

Figure 6. Aperture distribution for the Dixie Valley fracture. The left frame illustrates the overall aperture distribution, whereas the right frame focuses on the small-aperture distribution. For the numerical model, 25 microns were subtracted from each aperture value to enhance the effect of asperities. Flow is from right to left.
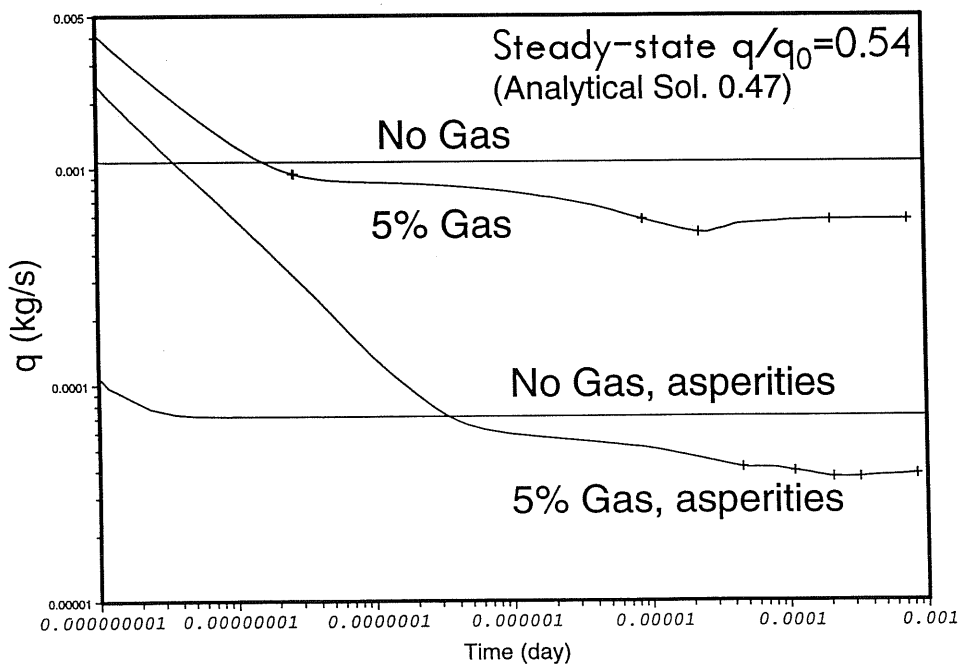

Figure 7. Flow rate as a function of time for two versions of the fracture model.
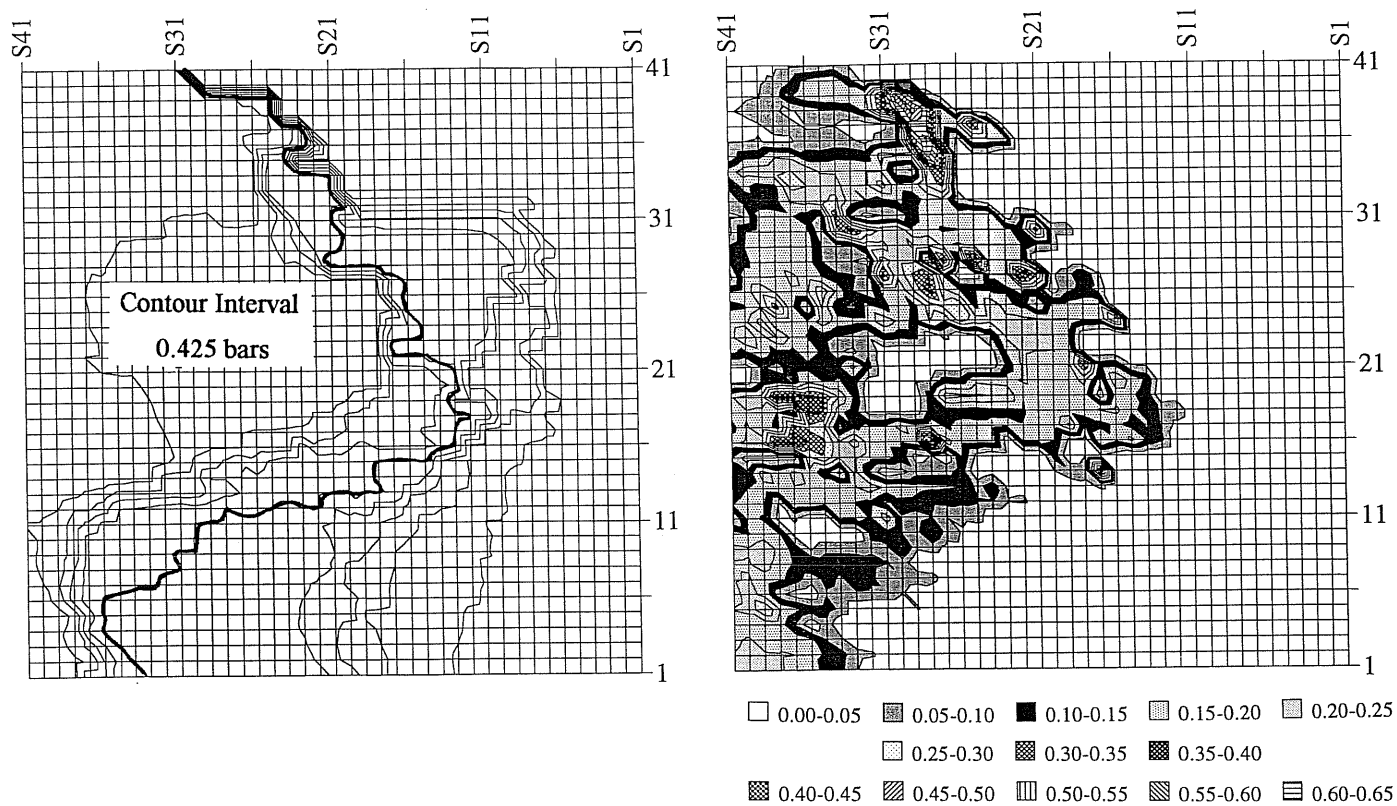
Figure 8. Modeled steady-state pressure (left) and gas saturation (right). Pressure is held fixed at 5 bars at the right edge and at 1 bar at the left edge. The bubble pressure is shown bold.
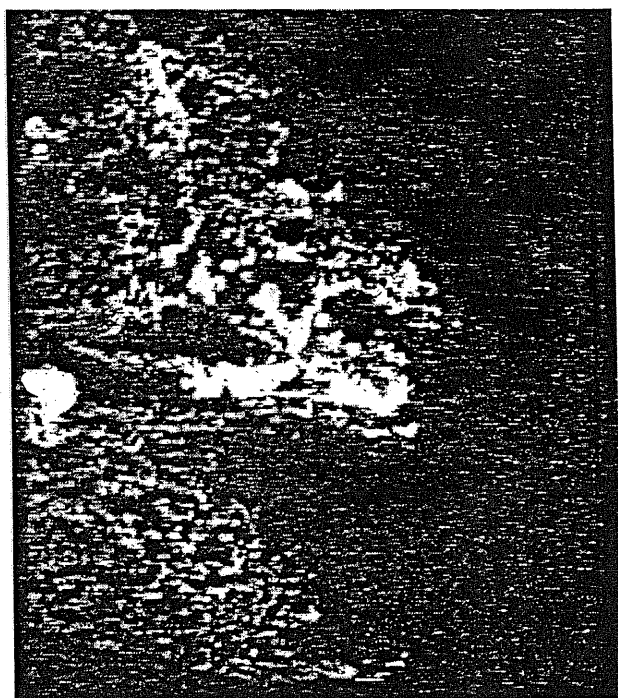
Contour Interval
0.425 bars

☐ 0.00-0.05   ▦ 0.05-0.10   ■ 0.10-0.15   ▨ 0.15-0.20   ▨ 0.20-0.25

▨ 0.25-0.30   ▦ 0.30-0.35   ▦ 0.35-0.40

▦ 0.40-0.45   ▨ 0.45-0.50   ⦀ 0.50-0.55   ▧ 0.55-0.60   ▤ 0.60-0.65

Figure 9. Observed steady-state gas distribution [white = gas, from *Geller et al.*, 1995].